



HAL
open science

The First High-contrast Images of X-Ray Binaries: Detection of Candidate Companions in the γ Cas Analog RX J1744.7-2713

M. Prasow-Émond, J. Hlavacek-Larrondo, K. Fogarty, J. Rameau, D. Mawet,
L.-S. Guité, P. Gandhi, A. Rao, J.F. Steiner, É. Artigau, et al.

► To cite this version:

M. Prasow-Émond, J. Hlavacek-Larrondo, K. Fogarty, J. Rameau, D. Mawet, et al.. The First High-contrast Images of X-Ray Binaries: Detection of Candidate Companions in the γ Cas Analog RX J1744.7-2713. *Astron.J.*, 2022, 164 (1), pp.7. 10.3847/1538-3881/ac6d57 . hal-03678650

HAL Id: hal-03678650

<https://hal.science/hal-03678650>

Submitted on 9 Mar 2023

HAL is a multi-disciplinary open access archive for the deposit and dissemination of scientific research documents, whether they are published or not. The documents may come from teaching and research institutions in France or abroad, or from public or private research centers.

L'archive ouverte pluridisciplinaire **HAL**, est destinée au dépôt et à la diffusion de documents scientifiques de niveau recherche, publiés ou non, émanant des établissements d'enseignement et de recherche français ou étrangers, des laboratoires publics ou privés.



Distributed under a Creative Commons Attribution 4.0 International License



The First High-contrast Images of X-Ray Binaries: Detection of Candidate Companions in the γ Cas Analog RX J1744.7-2713

M. Prasow-Émond^{1,2,†}, J. Hlavacek-Larrondo¹, K. Fogarty^{3,4}, J. Rameau^{2,5}, L.-S. Guité¹, D. Mawet^{3,6}, P. Gandhi⁷, A. Rao⁷, J. F. Steiner⁸, É. Artigau², D. Lafrenière^{1,2}, A. C. Fabian⁹, D. J. Walton⁹, L. M. Weiss¹⁰, R. Doyon^{1,2}, B. B. Ren (任彬)³, C. L. Rhea¹, T. Bégin¹, B. Vigneron¹, and M.-E. Naud²

¹Département de Physique, Université de Montréal, C.P. 6128, Succ. Centre-Ville, Montréal, QC H3C 3J7, Canada; myriam.prasow-emond@umontreal.ca

²Institute for Research on Exoplanets, Université de Montréal, Département de Physique, C.P. 6128 Succ. Centre-ville, Montréal, QC H3C 3J7, Canada

³Division of Physics, Math, and Astronomy, California Institute of Technology, Pasadena, CA, USA

⁴NASA Ames Research Center, Moffett Field, CA 94035, USA

⁵Univ. Grenoble Alpes, CNRS, IPAG, F-38000 Grenoble, France

⁶Jet Propulsion Laboratory, California Institute of Technology, Pasadena, CA 91109, USA

⁷Department of Physics and Astronomy, University of Southampton, Highfield, Southampton, SO17 1BJ, UK

⁸Harvard-Smithsonian Center for Astrophysics, Cambridge, MA 02138, USA

⁹Institute of Astronomy, Cambridge University, Madingley Road, Cambridge CB3 0HA, UK

¹⁰Department of Physics, University of Notre Dame, Notre Dame, IN 46556, USA

Received 2021 June 19; revised 2022 April 21; accepted 2022 May 4; published 2022 June 13

Abstract

X-ray binaries provide exceptional laboratories for understanding the physics of matter under the most extreme conditions. Until recently, there were few, if any, observational constraints on the circumbinary environments of X-ray binaries at ~ 100 – 5000 au scales. It remains unclear how the accretion onto the compact objects or the explosions giving rise to the compact objects interact with their immediate surroundings. Here, we present the first high-contrast adaptive optics images of X-ray binaries. These observations target all X-ray binaries within ~ 3 kpc accessible with the Keck/NIRC2 vortex coronagraph. This paper focuses on one of the first key results from this campaign; our images reveal the presence of 21 sources potentially associated with the γ Cassiopeiae analog high-mass X-ray binary RX J1744.7–2713. By conducting different analyses—a preliminary proper motion analysis, a color–magnitude diagram, and a probability of chance alignment calculation—we found that three of these 21 sources have a high probability of being bound to the system. If confirmed, they would be in wide orbits (~ 450 to 2500 au). While follow-up astrometric observations will be needed in ~ 5 – 10 yr to confirm further the bound nature of these detections, these discoveries emphasize that such observations may provide a major breakthrough in the field. In fact, they would be useful not only for our understanding of stellar multiplicity, but also for our understanding of how planets, brown dwarfs, and stars can form even in the most extreme environments.

Unified Astronomy Thesaurus concepts: Multiple stars (1081); Infrared astronomy (786); X-ray binary stars (1811); High mass x-ray binary stars (733); Coronagraphic imaging (313); Direct imaging (387)

1. Introduction

Exoplanets can exist in extreme environments; in fact, Wolszczan & Frail (1992) reported the discovery of a planetary system orbiting the millisecond pulsar PSR B1257+12. These planets were both the first confirmed exoplanets, as well as the first confirmed planets orbiting a compact object. In this system, the planets are small (from a fraction to a few M_{\oplus}) and in close orbits to the pulsar (up to a few astronomical units; hereafter au). Currently, there are just a few (~ 7) confirmed substellar companions orbiting pulsars (e.g., Bailes et al. 2017; Starovoit & Rodin 2017). These planets are thought to originate from a fallback disk postsupernovae in which they would have formed similarly as in protoplanetary disks (e.g., Yan et al. 2013), or simply from gravitational capture (e.g., Sigurdsson et al. 2003). Since then, thousands of exoplanets and brown dwarfs have been discovered with the advent of new, state-of-the-art instruments. These discoveries have bettered our

understanding of the solar system and have shown that planets and brown dwarfs can exist in a variety of environments: from hot Jupiters that orbit exceedingly close to their host star (e.g., Seager & Sasselov 1998; Evans et al. 2018) to planets found at orbital separations of up to several thousand au (e.g., Lafrenière et al. 2011; Naud et al. 2014). Overall, these discoveries emphasize that we still do not fully understand the conditions required for the formation of planets.

A recent study argued that substellar companions could even exist in extreme environments, such as X-ray binaries (Imara & Di Stefano 2018). These systems consist of a compact stellar remnant (white dwarf, neutron star, or black hole) accreting material from a donor star, and their interaction releases strong X-ray radiation (e.g., Tauris & van den Heuvel 2006). They have been extensively studied and monitored for several decades enabling a variety of major breakthroughs on accretion physics (e.g., Kara et al. 2019 for a recent example), as well as on the formation of outflows under extreme magnetic field conditions (see Fender et al. 2004 for a review). X-ray binaries are thus unique laboratories for studying a variety of astronomical phenomena under extreme conditions.

Although studies indicate that planets orbiting individual pulsars may be rare (e.g., Loehmer et al. 2004), a planet in close orbit to an X-ray binary could produce X-ray eclipses

[†] Corresponding author.



Table 1
Keck/NIRC2 Observing Log for RX J1744.7–2713^a

UT Date	2017 Sep 8	2020 Jul 11	2020 Jul 12
Filter	L'	L'	K_s
WFS	SH	py	py
Int. Time (s)	0.5	0.5	0.6
Coadds	60	60	45
Total frames	40	120	92
P. A. cov. (°)	14.3	38.3	39.6

Note.

^a Abbreviations: wave-front sensor (WFS), parallactic angle coverage (P. A. cov.)

detectable with current instruments (Imara & Di Stefano 2018). However, binary systems, such as X-ray binaries, may be more likely to host wide orbit companions (up to several hundred to thousand of au) because of planet–planet or planet–star interactions (e.g., Bonavita et al. 2016). Simulations also predict that giant planets and brown dwarfs can survive stellar explosions such as those undergone by X-ray binaries, but that these may tend to push out the companions to wider orbits (e.g., Welsh 2013). In this case, detecting substellar companions via transits or radial velocity shifts may not be optimal. In addition, in the case of high-mass X-ray binaries (HMXB), the companion star has not yet exploded, implying that the system should be fairly young (i.e., less than a few dozen Myr; e.g., Girardi et al. 1996). Substellar companions, if present, could therefore still be bright and amenable for detection via direct imaging (e.g., Burrows et al. 2001).

As part of a pilot study aiming to explore the immediate environments of X-ray binaries, we have obtained the first high-contrast adaptive optics images of X-ray binaries ideally suited for detecting companions that have formed in situ at large (~ 100 – 5000 au) radii or have been pushed out to large radii. These images consist of NIRC2 observations taken with Keck targeting all X-ray binaries within ~ 3 kpc.

Here, we present the first set of observations, targeting the γ Cassiopeiae-like HMXB harboring a Be donor star, RX J1744.7–2713. In Section 2, we present the observations and data reduction. In Section 3, we show the high-contrast images of RX J1744.7–2713, the background/foreground contaminant probability, the color–magnitude diagram, as well as how we determined the nature of the detections. In Section 4, we discuss our results and their implications, while in Section 5 we summarize and discuss future perspectives.

2. Observations and Data Reduction

2.1. RX J1744.7–2713

RX J1744.7–2713 (R.A.: $17^{\text{h}}44^{\text{m}}45^{\text{s}}.7659$; decl.: $-27^{\text{d}}13^{\text{h}}44^{\text{m}}.477$) is located at a distance of 1.22 ± 0.04 kpc (Gaia Collaboration et al. 2021) and was first identified as a HMXB by Israel et al. (1997). The distance above is based upon geometric parallax inversion and includes a zero-point offset correction of -0.0348 mas according to the algorithm described in Lindegren et al. (2021). Its optical component—HD 161103—has been spectroscopically characterized in Motch et al. (1997) and Lopes de Oliveira et al. (2006), and is classified as a Be star.

RX J1744.7–2713 has similar properties to γ Cassiopeiae (also known as 2S 0053+604; e.g., Raguzova & Popov 2005;

Shrader et al. 2015) and has an X-ray luminosity of $(3.08 \pm 0.49) \times 10^{32}$ erg s^{-1} (Naze & Motch 2018). Although the origin of X-ray emission in RX J1744.4–2713 is still debated, it may point to accretion onto a white dwarf (WD; Lopes de Oliveira et al. 2006).

It should be noted that in the case of Be stars, the star’s massive outflows lead to a diffuse and gaseous circumstellar disk known as a decretion disk (e.g., Kravtsov et al. 2020); however, these disks have radii at sub-au scales, which for RX J1744.7–2713 is well within the inner working angle of the NIRC2 vortex coronagraph.

In the case of RX J1744.4–2713, Coleiro & Chaty (2013) estimated the age of the system to be ~ 60 Myr by investigating the expected offset between the position of the Galaxy’s spiral arms and HMXBs. However, considering the uncertainties (e.g., see their Figure 13), the age of RX J1744.4–2713 is likely to be anywhere between a couple Myr to 80 Myr (95% confidence). Given these uncertainties, we consider the range of 5–60 Myr throughout this study and note that even if we were to consider an age outside this range, our conclusions remain the same.

Furthermore, the system has proper motions of -0.955 ± 0.100 mas yr^{-1} and -2.062 ± 0.077 mas yr^{-1} in R.A. and decl., respectively, and is located in the Galactic plane, as most of the HMXBs in our galaxy (e.g., Tauris & van den Heuvel 2006).

2.2. Observations

The Keck/NIRC2 vortex coronagraph (Mawet et al. 2005; Serabyn et al. 2016) was used to observe RX J1744.7–2713 in pupil-tracking mode—with the narrow-field camera (9.971 ± 0.004 mas/pixel; Service et al. 2016)—in L' -band in 2017 ($\lambda = 3.776$ μm , $\Delta\lambda = 0.700$ μm ; PI: Mawet) and in both L' -band and K_s -band in 2020 ($\lambda = 2.146$ μm , $\Delta\lambda = 0.311$ μm ; PI: Fogarty). Observations were adaptive-optics-assisted with the Keck II Shack-Hartmann wave-front sensor in 2017, which performs wave-front sensing in R , and the infrared pyramid wave-front sensor (PyWFS) in 2020, which performs wave-front sensing in H (Wizinowich et al. 2000; Bond et al. 2018). Given the R and H magnitudes of RX J1744.7–2713 ($R \sim 9$; Cutri et al. 2003, $H \sim 7$; Zacharias et al. 2012), the performances of the two wave-front sensors are comparable; however, we chose to use the PyWFS for our 2020 observations since sensing in H is advantageous for several extremely red HMXBs in our 2020 survey sample. Tip-tilt adjustments were performed with Quadrant Analysis of Coronagraphic Images for Tip-tilt sensing (Huby et al. 2017) in order to keep the star well centered on the vortex focal plane mask.

Individual exposure times, coadds, total number of frames and total integration times obtained for each observation are summarized in Table 1.

In our 2017 observations, we only obtained $\sim 14^\circ$ of field rotation, but in our 2020 observations we obtained $\sim 40^\circ$ of rotation in both bands to enable reduction using angular differential imaging (ADI; Marois et al. 2006). Additional frames taken with RX J1744.7–2713 moved off-axis were taken throughout each run to sample the evolution of the point-spread function (PSF) throughout the run and to obtain photometric measurements of RX J1744.7–2713.

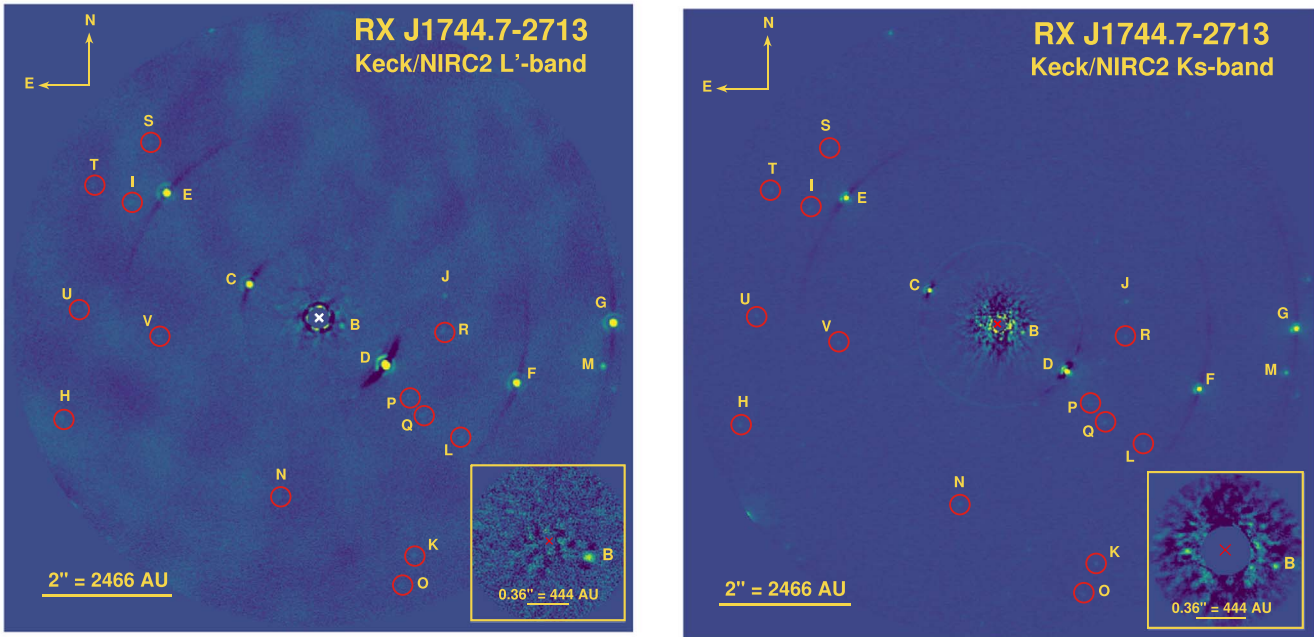


Figure 1. Left: Keck/NIRC2 L' high-contrast image of RX J1744.7–2713 acquired on 2020 July 11 and treated and reduced with a PCA annular ADI algorithm. The data were processed using VIP (Gomez Gonzalez et al. 2017). The 21 sources detected with $S/N > 5$ when computing the signal-to-noise map are labeled. The white X symbol denotes the position of the X-ray binary masked by the coronagraph. The inset at the bottom is a zoom on the central region to focus on the closest candidate at ~ 450 au. Right: Keck/NIRC2 K_s high-contrast image of RX J1744.7–2713 acquired on 2020 July 12. Labeled are the same objects detected from the L' image. The red X symbol denotes the position of the X-ray binary masked by the coronagraph.

2.3. Data Reduction

Data reduction (flat fielding, bad pixel masking, sky removal, image registration and selection, and centering via speckles) was performed using the Vortex Image Processing (VIP) package (Gomez Gonzalez et al. 2017). The frames were then derotated and mean combined, and a Principal Component Analysis (PCA) annular ADI algorithm from VIP was applied to obtain the high-contrast images (see Figure 1). Note that the number of principal components (n_{comp}) for each individual source was chosen to reach an optimal signal-to-noise ratio (S/N), by testing many values ranging from 1 to 50. We then generated the S/N and significance (signal in terms of σ ; Mawet et al. 2014) maps to identify sources with a S/N greater than 5 (which results in a signal greater than 4σ for all of our sources). This also provided estimates of the sources’ coordinates.

2.4. Magnitude Calculation

To calculate the full width at half maximum (FWHM) of the PSF for both filters, we fit a Gaussian profile to the median-collapsed PSF data cube. We obtained a FWHM of 83.2 milliarcseconds (hereafter mas) and 47.5 mas for L' and K_s , respectively. Note that we also generated a 2D synthetic PSF for L' flux fitting—using a Gaussian model and the corresponding FWHM—because of an artifact caused by thermal background noise from the primary mirror that has been folded back on-axis by the vortex phase mask. However, the use of a synthetic PSF does not affect the flux fitting much, as we get consistent results in the error bars when we test our K_s data with both real and synthetic PSFs.

Using the reduced data cube and the normalized and centered synthetic PSF, we injected fake companions with an inverse flux into the science data cube to estimate the

photometric counts, coordinates, and errors (Lagrange et al. 2010) of any detected source with a $S/N > 5$ in the L' S/N map. This process uses a Nelder–Mead optimization algorithm to find the coordinates and the flux of a source in a given aperture (a radius of 3 FWHM). We then divided the counts of the sources by the counts of the HMXB’s median-collapsed PSF data cube—measured in the same aperture as the sources—in order to obtain the flux of the candidate companion relative to the X-ray binary (i.e., the contrast).

Knowing the apparent magnitudes of RX J1744.7–2713 ($L' = 5.809 \pm 0.077$ mag and $K_s = 6.507 \pm 0.023$ mag; Cutri et al. 2003), the contrast can be converted to apparent magnitudes and absolute magnitudes (using the known distance in parsec), and then to mass using a model from MESA Isochrones and Stellar Tracks (MIST; Paxton et al. 2011, 2013, 2015, 2018; Choi et al. 2016; Dotter 2016; Faherty et al. 2016).

Servillat et al. (2012) reported that there is no significant variability in the light curve of HD 161103 (Be star in RX J1744.7–2713). However, large timescale (~ 50 – 100 yr) variability could still occur. We therefore injected a 5% additional error to the magnitudes to occur for any large timescale variability, and adding even larger errors does not change our results. As for the line-of-sight interstellar reddening $E(B - V)$, Schlafly & Finkbeiner (2011) estimated it to be $E(B - V) \sim 3.4$. Since the extinction $A(V)$ is related to $E(B - V)$ via $A(V) = 3.2E(B - V)$, we have $A(V) \sim 10.9$, and assuming a typical extinction power law varying as $A(V) \propto \lambda^{-1.75}$ (Draine 1989; and see Doherty et al. 1994; Viehmann et al. 2005; Dong et al. 2017; Uyama et al. 2020 for examples of papers that use that technique), we obtain $A(K_s) \sim 0.85$ and $A(L') \sim 0.32$ (via a simple cross product). Therefore, K_s and L' are not strongly impacted by dust reddening; such an extinction results in a color shift of

~ 0.5 mag for $K_s - L'$ and a magnitude shift of ~ 0.3 for L' . These corrections have been applied to our results; by adding them to the K_s and L' magnitudes.

2.5. Injection/Recovery

In order to estimate the errors on the parameters—the flux and the position (i.e., the separation from the XRB in mas and the parallactic angle in degrees)—obtained with the optimization process, we proceeded by injection recovery. We first injected fake companions with known values for the parameters, and then ran the optimization code to compare the outputs with the known inputs. For each parameter, we tested this method for 90 different values, with a range covering the values of the true candidate companions of the system. We found that the errors were relatively stable while increasing the values of the parameters, meaning they are more significant for smaller values within the range. Averaging the results, we obtained errors of the order of ~ 0.5 mas for the separation and $\sim 0.01^\circ$ for the parallactic angle. As for the flux, we considered only the errors explained in Section 2.4, as they are dominant and physically significant.

The injection/recovery method gives relatively small errors, but other types of error must be included (e.g., the error when determining the center of the vortex coronagraph within the different frames). As our 2020 L' and K_s observations are spaced out by only one day, the astrometry parameters should be the same. Therefore, we also considered the difference between our 2020 L' and K_s results as part of astrometry errors, which are greater than the injection/recovery errors.

3. Companion Candidates

3.1. High-contrast Images

The left panel of Figure 1 presents the L' high-contrast image of RX J1744.7–2713, while the right panel shows the K_s image, both from the 2020 observation runs. The L' image from 2017 is shown in Figure A1 in the Appendix, in which only three sources are detected. With deeper observations in 2020 (unlike the poor parallactic coverage for angular differential imaging in 2017), it revealed a then-unresolved ~ 450 au candidate companion from the central X-ray binary. We therefore only consider the 2020 observations for the remainder of the paper, except for a preliminary proper motion analysis in Section 3.4.

Using the L' S/N map, we find a total of 21 sources that have a $S/N > 5$. These sources are labeled from B to V in Figure 1 and are also detected in the K_s image with a $S/N > 5$. Moreover, as the K_s image is more sensitive (more sources), note that we only considered the sources detected in L' when measuring the magnitudes, since potential substellar companions are usually brighter in L' (Faherty et al. 2016). The projected separations from RX J1744.7–2713, estimated using the distance and the plate scale, range from ~ 450 to ~ 5500 au. In the next sections, we examine the nature of these sources via different analyses.

3.2. Background Source Contamination

3.2.1. TRILEGAL

To assess the possibility that the field of view may be dominated by background or foreground sources, we derived an estimation of the expected number of sources for the field of

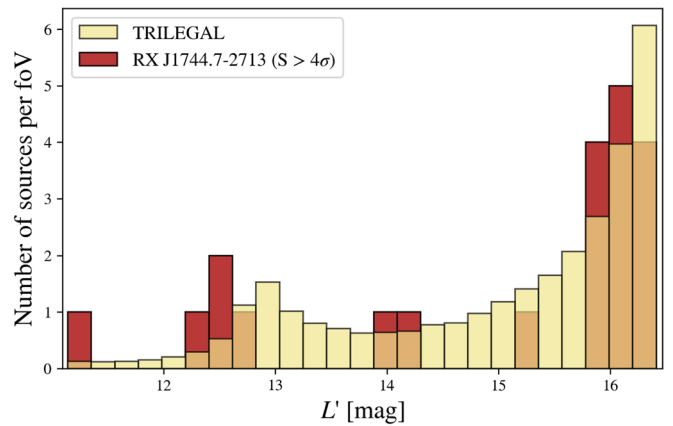


Figure 2. L' distribution for RX J1744.7–2713 (red) and for the sources simulated by TRILEGAL (yellow). The orange color is where the two distributions are superposed.

view using TRILEGAL—a 3D model used for simulating the stellar photometry of any Galaxy field (Girardi et al. 2005; and see Chun et al. 2015; Dietrich & Ginski 2018; Jones et al. 2021; Williams et al. 2021 for examples of papers that use this model). Constraining the model to the faintest detected magnitude in L' , we calculated the expected number of sources for the entire field of view (i.e., $10''24 \times 10''24$). Figure 2 presents the distribution of the L' magnitude for the simulated sources and for RX J1744.7–2713.

We first conducted a Kolmogorov–Smirnov test to assess the possibility that the two distributions follow the same statistical function. Regardless of the horizontal binning size, we obtain a very small probability ($\ll 0.1$) of observing the same distribution. Therefore, we can reject the null hypothesis and conclude that at least one of the sources is likely to be bound. However, we note that for fainter magnitudes, the distributions are roughly similar, so the corresponding sources are likely unrelated sources. On the contrary, there is a larger proportion of brighter objects than predicted by TRILEGAL. We thus conclude that the brighter sources in RX J1744.7–2713 (C, D, E, F, and G in Figure 1) are less likely to be contaminants, as their presence is not explained by the model. However, this method is not precise and is only intended to provide a first rough estimate.

3.2.2. Probability of Chance Alignment

In addition to TRILEGAL, we derived a probability of chance alignment—i.e., the likelihood that the candidates are not bound to the system—using the Two Micron All-Sky Survey (2MASS) Point Source Catalog (PSC; see Correia et al. 2006; Lafrenière et al. 2008, 2014 for examples of that technique). More specifically, we retrieved all the sources in a $15' \times 15'$ field surrounding RX J1744.7–2713, and we constructed a cumulative distribution of the number of sources as a function of the apparent K_s magnitude. We then divided this result by the area (in arcsec^2) to obtain a surface density Σ that depends on the limiting magnitude of the candidate, i.e., $\Sigma = \Sigma(K_s < K_{s,\text{candidate}})$. Assuming a random uniform Poisson distribution of unrelated objects across the chosen area, the probability that a candidate is not related to the system is given by:

$$P_{\text{unrelated}}(\Sigma, \Theta) = 1 - \exp(-\pi\Sigma\Theta^2) \quad (1)$$

Table 2

Probability of Unrelation with RX J1744.7–2713 for All the Sources (B to V in Figure 1), as Estimated from 2MASS PSC

Source	Σ (arcsec ⁻²)	Θ (arcsec)	$1 - P_{\text{unrelated}}(\Sigma, \Theta)$ (%)
B	3.24×10^{-2}	0.37	98.6
C	2.11×10^{-2}	1.18	91.2
D	7.14×10^{-3}	1.25	96.6
E	1.66×10^{-2}	3.02	62.3
F	2.47×10^{-2}	3.19	45.5
G	2.43×10^{-2}	4.51	21.2
H	3.29×10^{-2}	4.23	15.8
I	3.29×10^{-2}	3.37	30.9
J	3.29×10^{-2}	1.96	67.3
K	3.29×10^{-2}	3.93	20.2
L	3.29×10^{-2}	2.85	43.2
M	3.29×10^{-2}	4.42	13.4
N	3.29×10^{-2}	2.80	44.4
O	3.29×10^{-2}	4.29	14.9
P	3.29×10^{-2}	1.83	70.6
Q	3.29×10^{-2}	2.18	61.3
R	3.29×10^{-2}	1.91	68.6
S	3.29×10^{-2}	3.74	23.6
T	3.29×10^{-2}	4.02	18.9
U	3.29×10^{-2}	3.69	24.5
V	3.29×10^{-2}	2.48	53.1

where Θ is the projected separation from RX J1744.7–2713 (in arcsec). Table 2 shows the Σ , Θ , and $1 - P_{\text{unrelated}}(\Sigma, \Theta)$ values for all sources (B to V).

This table shows that sources B, C, D have a high probability of not being unrelated to the system, respectively, of 98.6%, 91.2%, and 96.6%, which is consistent with Figure 5. Moreover, sources E, J, P, Q, and R have high but less convincing probabilities, while the remaining sources are likely to be background stars since their probability is lower than 60%.

3.3. Color–Magnitude Diagram

Since both L' and K_s observations were taken, we were able to construct a color–magnitude diagram, as has been done in previous studies to estimate the physical properties of companions (e.g., Rameau et al. 2013; Salaris & Bedin 2018; Jones et al. 2021). Figure 3 presents the absolute magnitude in L' versus $K_s - L'$ for the 21 potential companions to RX J1744.7–2713. The track from MIST at 10 Myr is overlaid, as well as the extinction vector (see Section 2.4).

From this diagram, the fainter sources (H to L and O to V) could be coherent with low-mass stars (M- or K-type), while B and M could be G-type stars. Moreover, B, C, E, F, and G have estimated masses potentially coherent with massive A- or B-type stars. Due to their offset $K_s - L'$ color, the other sources (F, G, M) seem to be inconsistent with being substellar or stellar companions, and may therefore be unrelated background objects such as extincted background stars or artifacts.

A table with the position, the L' and K_s magnitudes, the estimated mass, and the projected separation of the 21 sources companion candidates is presented in the Appendix (see Table A1). Note that the masses were estimated from the 5–60 Myr stated in Section 2.1 and that we did not apply the extinction correction for this table.

Thus, RX J1744.7–2713 does not currently show evidence of exoplanet-mass companions, as the candidate companions have masses from ~ 0.2 to $6 M_{\odot}$. However, we reached excellent S/N and we detected sources down to $L' \sim 16.5$. Another way to gather more information on the sources is via additional bands (e.g., H) or via spectroscopic characterization.

3.4. Preliminary Proper Motion Analysis

To confirm more robustly that the sources are bound, a proper motion analysis could be conducted (e.g., Marois et al. 2008). Given the distance (~ 1 kpc) and proper motion of RX J1744.7–2713 (see Section 2.1), a $>3\sigma$ detection will only be possible in ~ 5 – 10 yr. However, considering that there is a three-year interval between our 2017 and 2020 sets of observations, a preliminary proper motion analysis was conducted for sources C, D, and J. The plots of astrometric positions (position angle in degrees, separation in mas, and relative separations in R.A. and decl.) for each of these sources relative to the X-ray binary can be found in the Appendix (see Figure A2). Accounting for the errors from Section 2.5, we conclude that both scenarios—stationary background or comoving with RX J1744.7–2713—are possible for sources D and J at this current epoch. We note that the position of source C is offset from the tracks, which indicates that it could be a nonstationary background object.

3.5. Stability of the Wide Orbits

The 21 sources detected in RX J1744.7–2713 at high S/N would have wide projected separations (from ~ 450 to ~ 5500 au), which raises concerns as to whether potential companions could be gravitationally bound to the system. However, very large separations have been observed in many known systems including companions white dwarfs or other evolved systems (e.g., 2000 au for GU Psc b; Naud et al. 2014; 2985 au for WISE 2005+5424; Mace et al. 2013; 16 500–26 500 au for LSPM 1459+0857 AB; Day-Jones et al. 2011). Baron et al. (2019) reported that the occurrence of substellar companions at very large orbits are rare. However, in RX J1744.7–2713 the mass ratios are small (from $q \sim 0.003$ to ~ 0.08), and such ratios have yet to be studied in detail. Despite the large separations, the large mass of the central system (i.e., the X-ray binary) implies a high binding energy. Assuming a total mass M_{XRB} of $\sim 18 M_{\odot}$ for RX J1744.7–2713 (typical masses for WD and Be stars) and a mass M_c of $\sim 80 M_{\text{Jup}}$ as a lower limit for the companions, we can estimate the binding energy of the system via the following equation (assuming circular orbits):

$$E_{\text{bind}} \sim -\frac{GM_{\text{XRB}}M_c}{1.27r}. \quad (2)$$

Here, 1.27 is the average projection factor between r and the semimajor axis, assuming a random viewing angle (e.g., Brandeker et al. 2006). We obtain $E_{\text{bind}} \sim -4.3 \times 10^{43}$ erg and $E_{\text{bind}} \sim -3.2 \times 10^{42}$ erg for the closest (450 au) and farthest (5500 au) candidates, respectively. In both cases, the binding energy is higher than in many known bound systems (e.g., $\sim 10^{41}$ erg; Naud et al. 2014).

Therefore, it is not unreasonable that the multiple stellar companion candidates, if confirmed with proper motion analysis, are gravitationally bound to the HMXB despite their wide separations. However, it is important to note that it is unlikely that all these sources would be bound due to dynamic instability. In fact, although we do not have detailed

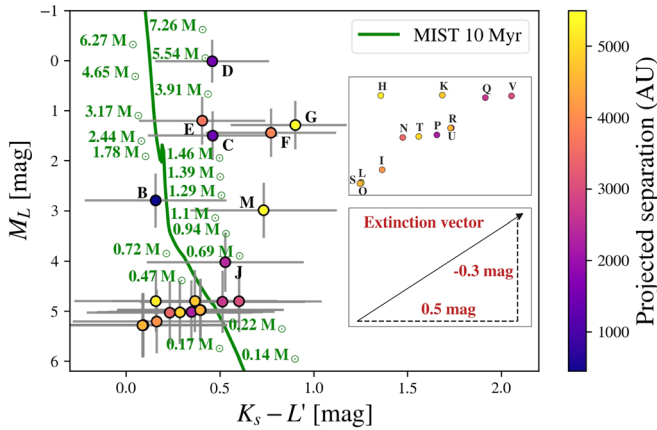


Figure 3. Absolute magnitude in L' vs. $K_s - L'$ color for the 21 companion candidates (colored circles) in RX J1744.7–2713. The colorbar indicates the projected separation (in au) from the X-ray binary. Overlaying is the MIST evolutionary track for stars at 10 Myr (Paxton et al. 2011, 2013, 2018, 2015; Choi et al. 2016; Dotter 2016; Faherty et al. 2016). The inset at the top right is a close-up of the fainter sources. The inset at the bottom right shows the extinction vector, i.e., the shift in magnitude and color caused by extinction (corrections have already been applied).

information on their potential orbital motion yet, candidate companions C and D have similar separations from RX J1744.7–2713, and simulations show that this configuration can be unstable (e.g., Kiseleva et al. 1994). On the contrary, a scenario of a triple system—composed of the X-ray binary (considered as one system here), candidate companion B, and candidate companion C, D, E or J—is more plausible according to basic N -body simulations.

4. Discussion

These analyses allowed us to reject most of the 21 sources as candidate companions. Until a more significant proper motion analysis can be undertaken, we consider sources B, D, and J to be strong candidates of stellar companions bound to RX J1744.7–2713 and we discuss the implications of these results in the following section.

4.1. Stellar Multiplicity

The discovery of multiple probable stellar candidate companions in RX J1744.7–2713 implies that it would be a multiple-star system. In fact, high order multiplicity increases with primary mass (e.g., Peter et al. 2012), and although surveys are incomplete, they suggest that stellar multiplicity is frequent in high-mass stars, such as young B stars (see Duchêne & Kraus 2013 for a review on stellar multiplicity). More precisely, if we consider only the confirmed companions, the multiplicity frequency would be $\geq 80\%$ for stars with a mass $\geq 16 M_\odot$ (e.g., Chini et al. 2012). Regarding the companion frequency (i.e., the average number of companion per target in a population), it is $\approx 130 \pm 20\%$ for high-mass stars (Duchêne & Kraus 2013). Moreover, the frequency $N(n)$ of multiplicity n roughly follows a geometric distribution $N(n) \propto 2.3^{-n}$ (up to $n = 7$; Eggleton & Tokovinin 2008) for solar-type stars; however, there is currently no derived relation for massive stars. As RX J1744.7–2713 is already a known high-mass binary system, the complete sample of this project could therefore enable us to better understand if X-ray binaries

are likely to stellar multiplicity, as well as probing stellar multiplicity at mass ratios below ~ 0.1 .

4.2. Similarities to γ Cassiopeiae

In addition, RX J1744.7–2713 is a γ Cassiopeiae analog, and the latter has two faint optical companions (e.g., Mason et al. 2001). Therefore, it suggests that Be stars might be more favorable to stellar multiplicity. As γ Cassiopeiae is a HMXB candidate (e.g., Haberl 1995), it also means that stellar companions could be common in X-ray binaries.

4.3. Formation Scenarios

In the case of X-ray binaries, companions are believed to form (1) from the direct fragmentation of a collapsing prestellar core, i.e., roughly at the same time as the stars that will eventually form the X-ray binary (e.g., Bate 2012), (2) from the circumbinary disk surrounding the initial binary system (i.e., preexplosion of the then-compact object; e.g., Kratter et al. 2010), or (3) from the supernova fallback disk surrounding the X-ray binary (postexplosion; e.g., Wolszczan & Frail 1992). Note that fallback disks could lead to the formation of substellar companions, but they are not massive enough to allow star formation. However, this work does not show evidence of such disks, so we can not conclude how the candidate companions have formed. Furthermore, if companions are formed under the last scenario, then they must be younger than the X-ray binary; their age could be lower than 5 Myr (the lower limit for RX J1744.7–2713’s age stated in Section 2.1). Overall, X-ray binaries could host multigeneration companions that form at different epochs through the evolution of the binary. This work explores the idea that the interactions between X-ray binaries and their surroundings might be complex, leading to multiple companions and hierarchical orbits. Moreover, it opens up the discussion on how substellar and stellar formation could occur even in the most extreme environments.

5. Summary and Conclusions

In this work, we have shown the first high-contrast images of the γ Cas analog RX J1744.7–2713, using observations from the Keck/NIRC2 vortex coronagraph. These images reveal the presence of 21 sources detected with a $S/N > 5$. From a combination of various analyses, we found that three of these sources are strong candidates as stellar companions, and that they would be in wide orbits (~ 450 to 2500 au). Follow-up observations will be needed in ~ 5 – 10 yr to conduct a more significant proper motion analysis and confirm the nature of these detections. We also aim to obtain the spectrum of the sources in order to assess the nature of the sources. If confirmed, these results have direct implications for our understanding of how multiple-star systems form and how X-ray binaries may actually not be simple binary systems. These observations are part of a pilot study aiming to provide direct imaging for all X-ray binaries within ~ 3 kpc accessible with Keck/NIRC2. To date, 14 X-ray binaries have been observed, and the remaining results will be presented in a future paper (M. Prasow-Émond et al. 2022, in preparation).

The data presented herein were obtained at the W. M. Keck Observatory, which is operated as a scientific partnership among the California Institute of Technology, the University of

California, and the National Aeronautics and Space Administration. The Observatory was made possible by the generous financial support of the W. M. Keck Foundation. The authors wish to recognize and acknowledge the very significant cultural role and reverence that the summit of Maunakea has always had within the indigenous Hawaiian community. We are most fortunate to have the opportunity to conduct observations from this mountain. We also want to thank V. Christiaens for the help with VIP.

M.P.E. is supported by the Institute for Data Valorisation (IVADO) through the M. Sc. Excellence Scholarship, by the Department of Physics of the Université de Montréal and by the Institute for Research on Exoplanets (iREx). J.H.L. is supported by the Natural Sciences and Engineering Research Council of Canada (NSERC) through the Canada Research Chair programs and wishes to acknowledge the support of an NSERC Discovery Grant and the NSERC accelerator grant. J.R. acknowledges support by the French National Research Agency in the framework of the Investissements d’Avenir program (ANR-15-IDEX-02), through the funding of the “Origin of Life” project of the Univ. Grenoble-Alpes. D.J.W. acknowledges financial support from STFC in the form of an Ernest Rutherford fellowship.

Appendix

This Appendix presents additional data related to the main text. Figure A1 shows the L’-band high-contrast image of RX J1744.7-2713 obtained during the 2017 observation night. Figure A2 presents the preliminary proper motion analysis plots—i.e., the position angle in degree and the separation in mas as a function of time, and the relative separations from the

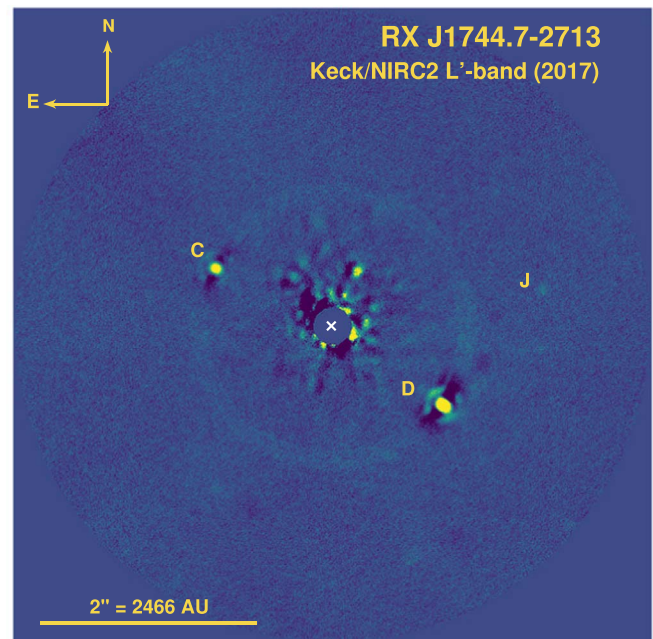


Figure A1. Keck/NIRC2 L' high-contrast image of RX J1744.7–2713 acquired on September 08 2017 and treated and reduced with a PCA annular ADI algorithm (Gomez Gonzalez et al. 2017). Labeled are the sources detected with a $S/N > 5$, using the same labels from Figure 1. The white X symbol denotes the position of the X-ray binary masked by the coronagraph.

X-ray binary in R.A. and decl.—between two epochs (2017 September 8 and 2020 July 11) for three sources (C, D, and J). Table A1 presents the calculated physical properties for the 21 sources.

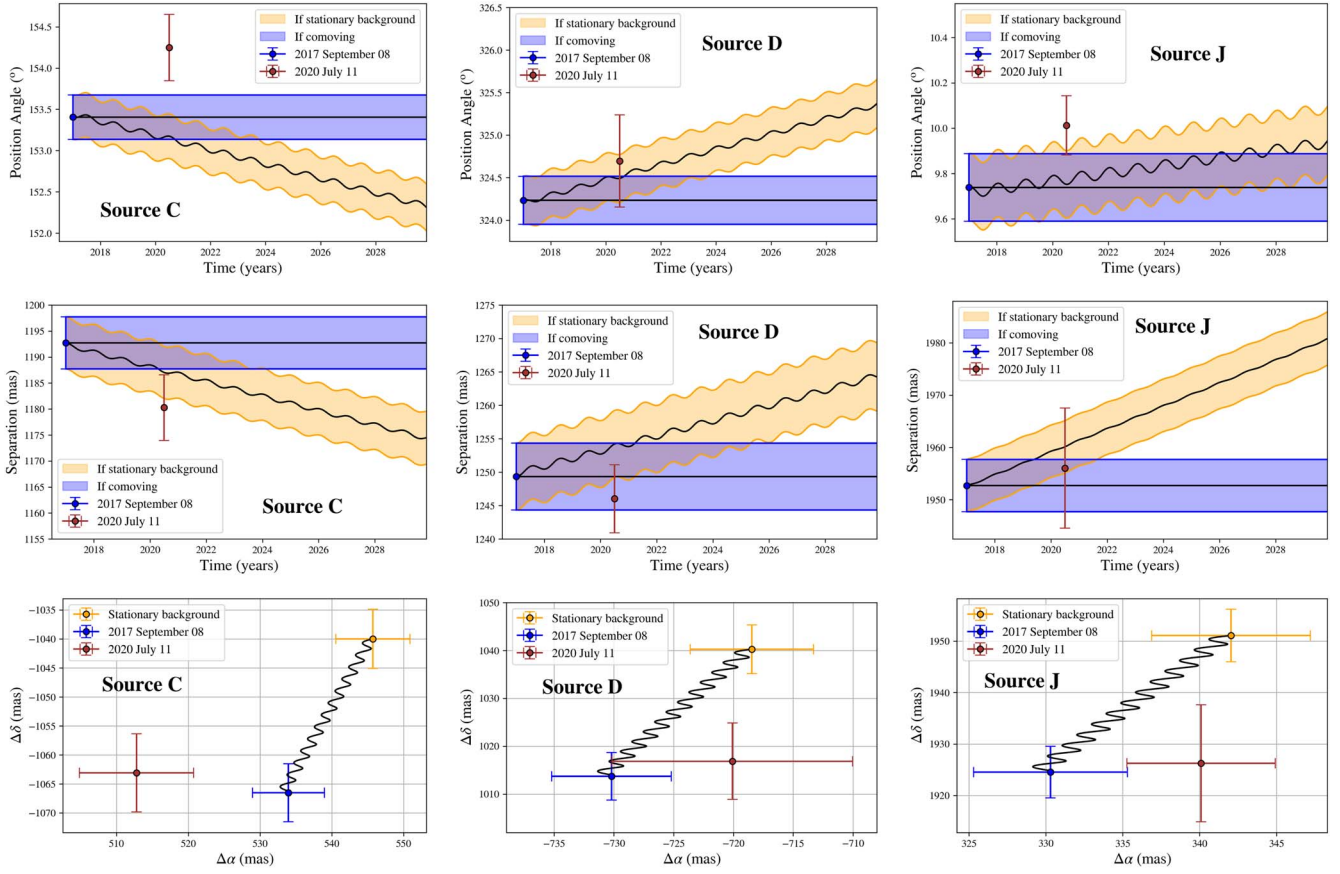


Figure A2. Top row: position angle in degrees of the sources C (left), D (middle), and J (right) relative to its host, as measured by Keck/NIRC2 on 2017 September 08 (blue data point). The red data point is the position angle measured by Keck/NIRC2 on 2020 July 11. An infinitely distant background object with zero proper motion would be following the orange track, while a comoving companion would lie within the blue area. Middle row: same as the top row, but for the separation from the X-ray binary in mas. Bottom row: relative separations between the source and the X-ray binary in R.A. (α) and decl. (δ). The first epoch astrometric point is plotted in blue (2017 September 08), while the second epoch astrometric point is plotted in red (2020 July 11). The expected position for a background object is plotted in yellow, along with a proper and parallactic motion track.

Table A1
Physical Properties of the 21 Sources in RX J1744.7–2713

Source	n_{comp}	r (mas)	P.A. (deg)	L' (mag)	K_s (mag)	Estimated mass (M_{\odot})	Projected separation (au)
B	14	368 ± 4	340.5 ± 1.4	13.5 ± 0.7	13.2 ± 0.7	0.9–1.2	449
C	4	1180 ± 6	154.2 ± 0.4	12.2 ± 0.6	12.2 ± 0.6	1.7–2.2	1440
D	2	1246 ± 5	324.7 ± 0.5	10.7 ± 0.5	10.7 ± 0.5	4.1–4.8	1520
E	5	3018 ± 2	140.6 ± 0.2	11.9 ± 0.6	11.8 ± 0.6	2.5–2.6	3681
F	15	3189 ± 7	341.8 ± 0.2	12.2 ± 0.6	12.4 ± 0.6	1.8–2.2	3890
G	29	4506 ± 12	359.1 ± 0.1	12.0 ± 0.6	12.4 ± 0.6	1.9–2.4	5497
H	25	4228 ± 9	201.34 ± 0.09	15.5 ± 0.8	15.2 ± 0.8	0.2–0.6	5158
I	16	3369 ± 4	148.4 ± 0.1	15.9 ± 0.8	15.6 ± 0.8	0.1–0.5	4110
J	16	1956 ± 12	10.0 ± 0.1	14.8 ± 0.7	14.8 ± 0.7	0.3–0.8	2386
K	28	3933 ± 10	291.9 ± 0.3	15.5 ± 0.8	15.4 ± 0.8	0.2–0.6	4798
L	8	2851 ± 1	320.1 ± 0.2	16.0 ± 0.8	15.6 ± 0.8	0.1–0.5	3478
M	33	4416 ± 5	350.3 ± 0.1	13.7 ± 0.7	14.0 ± 0.7	0.8–1.1	5387
N	7	2803 ± 5	257.5 ± 0.2	15.8 ± 0.8	15.5 ± 0.8	0.2–0.5	3419
O	25	4291 ± 8	287.0 ± 0.3	16.0 ± 0.8	15.6 ± 0.8	0.1–0.5	5235
P	21	1835 ± 8	319.0 ± 0.2	15.8 ± 0.8	15.6 ± 0.8	0.2–0.5	2238
Q	20	2176 ± 16	316.5 ± 0.6	15.5 ± 0.8	15.6 ± 0.8	0.2–0.6	2655
R	26	1910 ± 17	354.18 ± 0.09	15.7 ± 0.8	15.6 ± 0.8	0.2–0.5	2331
S	22	3737 ± 15	133.95 ± 0.05	16.0 ± 0.8	15.6 ± 0.8	0.1–0.5	4559
T	32	4016 ± 9	149.5 ± 0.1	15.8 ± 0.8	15.5 ± 0.8	0.2–0.5	4899
U	17	3689.3 ± 0.2	177.87 ± 0.01	15.7 ± 0.8	15.6 ± 0.8	0.2–0.5	4501
V	8	2475 ± 18	186.6 ± 0.1	15.5 ± 0.8	15.6 ± 0.8	0.2–0.6	3020

Note. Where r is the Radial Separation from the X-ray Binary in Mas, P.A. is the Position Angle in the image in Degrees, and L' and K_s are the Apparent Magnitudes (see Section 2.5 for Errors). No extinction correction was applied (see Section 2.4). The second column is the optimal number of principal components used for the fitting.

ORCID iDs

M. Prasow-Émond  <https://orcid.org/0000-0002-2457-3431>
 J. Hlavacek-Larrondo  <https://orcid.org/0000-0001-7271-7340>
 K. Fogarty  <https://orcid.org/0000-0002-2691-2476>
 J. Rameau  <https://orcid.org/0000-0003-0029-0258>
 L.-S. Guité  <https://orcid.org/0000-0002-8323-7809>
 D. Mawet  <https://orcid.org/0000-0002-8895-4735>
 P. Gandhi  <https://orcid.org/0000-0003-3105-2615>
 J. F. Steiner  <https://orcid.org/0000-0002-5872-6061>
 É. Artigau  <https://orcid.org/0000-0003-3506-5667>
 D. Lafrenière  <https://orcid.org/0000-0002-6780-4252>
 A. C. Fabian  <https://orcid.org/0000-0002-9378-4072>
 D. J. Walton  <https://orcid.org/0000-0001-5819-3552>
 L. M. Weiss  <https://orcid.org/0000-0002-3725-3058>
 R. Doyon  <https://orcid.org/0000-0001-5485-4675>
 B. B. Ren (任彬)  <https://orcid.org/0000-0003-1698-9696>
 C. L. Rhea  <https://orcid.org/0000-0003-2001-1076>
 T. Bégin  <https://orcid.org/0000-0002-5837-8618>
 B. Vigneron  <https://orcid.org/0000-0002-2478-5119>
 M.-E. Naud  <https://orcid.org/0000-0003-1807-1598>

References

- Bailes, M., Bates, S. D., Bhalerao, V., et al. 2011, *Sci*, **333**, 1717
 Baron, F., Lafrenière, D., Artigau, É., et al. 2019, *AJ*, **158**, 187
 Bate, M. R. 2012, *MNRAS*, **419**, 3115
 Bonavita, M., Desidera, S., Thalmann, C., et al. 2016, *A&A*, **593**, A38
 Bond, C. Z., Wizinowich, P., Chun, M., et al. 2018, *Proc. SPIE*, **10703**, 107031Z
 Brandeker, A., Jayawardhana, R., Khavari, P., et al. 2006, *ApJ*, **652**, 1572
 Burrows, A., Hubbard, W. B., Lunine, J. I., & Liebert, J. 2001, *RvMP*, **73**, 719
 Chini, R., Hoffmeister, V. H., Nasserri, A., et al. 2012, *MNRAS*, **424**, 1925
 Choi, J., Dotter, A., Conroy, C., et al. 2016, *ApJ*, **823**, 102
 Chun, S.-H., Jung, M., et al. 2015, *A&A*, **578**, A51
 Coleiro, A., & Chaty, S. 2013, *ApJ*, **764**, 185
 Correia, S., Zinnecker, H., Ratzka, T., et al. 2006, *A&A*, **459**, 909
 Cutri, R. M., Skrutskie, M. F., van Dyk, S., et al. 2003, *yCat*, **II/246**
 Day-Jones, A. C., Pinfield, D. J., Ruiz, M. T., et al. 2011, *MNRAS*, **410**, 705
 Dietrich, J., & Ginski, C. 2018, *A&A*, **620**, A102
 Doherty, R. M., Puxley, P., Doyon, R., et al. 1994, *MNRAS*, **266**, 497
 Dong, H., Schödel, R., Williams, B. F., et al. 2017, *MNRAS*, **471**, 3617
 Dotter, A. 2016, *ApJS*, **222**, 8
 Draine, B. T. 1989, *ESASP*, **22**, 93
 Duchêne, G., & Kraus, A. 2013, *ARA&A*, **51**, 269
 Eggleton, P. P., & Tokovinin, A. A. 2008, *MNRAS*, **389**, 869
 Evans, T. M., Sing, D. K., Goyal, J. M., et al. 2018, *AJ*, **156**, 283
 Faherty, J. K., Riedel, A. R., Cruz, K. L., et al. 2016, *ApJS*, **225**, 10
 Fender, R. P., Belloni, T. M., & Gallo, E. 2004, *MNRAS*, **355**, 1105
 Gaia Collaboration, Brown, A. G. A., Vallenari, A., et al. 2021, *A&A*, **649**, A1
 Girardi, L., Bressan, A., Chiosi, C., et al. 1996, *A&AS*, **117**, 113
 Girardi, L., Groenewegen, M. A. T., Hatziminaoglou, E., & da Costa, L. 2005, *A&A*, **436**, 895
 Gomez Gonzalez, C. A., Wertz, O., Absil, O., et al. 2017, *AJ*, **154**, 7
 Haberl, F. 1995, *A&A*, **296**, 685
 Huby, E., Bottom, M., Femenia, B., et al. 2017, *A&A*, **600**, A46
 Imara, N., & Di Stefano, R. 2018, *ApJ*, **859**, 40
 Israel, G. L., Stella, L., Angelini, L., et al. 1997, *ApJL*, **474**, L53
 Jones, O. C., Nally, C., Sharp, M. J., et al. 2021, *MNRAS*, **504**, 565
 Kara, E., Steiner, J. F., Fabian, A. C., et al. 2019, *Natur*, **565**, 198
 Kiseleva, G., Eggleton, P. P., & Anosova, J. P. 1994, *MNRAS*, **267**, 161
 Kratter, K. M., Matzner, C. D., Krumholz, M. R., & Klein, R. I. 2010, *ApJ*, **708**, 1585
 Kravtsov, V., Berdyugin, A. V., Piirola, V., et al. 2020, *A&A*, **643**, A170
 Lafrenière, D., Jayawardhana, R., Brandeker, A., Ahmic, M., & van Kerkwijk, M. H. 2008, *ApJ*, **683**, 844
 Lafrenière, D., Jayawardhana, R., Janson, M., et al. 2011, *ApJ*, **730**, 42
 Lafrenière, D., Jayawardhana, R., van Kerkwijk, M. H., Brandeker, A., & Janson, M. 2014, *ApJ*, **785**, 47
 Lagrange, A. M., Bonnefoy, M., Chauvin, G., et al. 2010, *Sci*, **329**, 57
 Lindgren, L., Bastian, U., Biermann, M., et al. 2021, *A&A*, **649**, A4
 Loehmer, O., Wolszczan, A., & Wielebinski, R. 2004, *A&A*, **425**, 763
 Lopes de Oliveira, R., Motch, C., Haberl, F., Negueruela, I., & Janot-Pacheco, E. 2006, *A&A*, **454**, 265
 Mace, G. N., Kirkpatrick, J. D., Cushing, M. C., et al. 2013, *ApJ*, **777**, 36
 Marois, C., Lafrenière, D., Doyon, R., et al. 2006, *ApJ*, **641**, 556
 Marois, C., Macintosh, B., Barman, T., et al. 2008, *Sci*, **322**, 1348
 Mason, B. D., Wycoff, G. L., Hartkopf, W. I., Douglass, G. G., & Worley, C. E. 2001, *AJ*, **122**, 3466
 Mawet, D., Milli, J., Wahhaj, Z., et al. 2014, *ApJ*, **792**, 97
 Mawet, D., Riaud, P., Absil, O., & Surdej, J. 2005, *ApJ*, **633**, 1191
 Motch, C., Haberl, F., Dennerl, K., Pakull, M., & Janot-Pacheco, E. 1997, *A&A*, **323**, 853
 Naud, M.-E., Artigau, É., Malo, L., et al. 2014, *ApJ*, **787**, 5
 Naze, Y., & Motch, C. 2018, *A&A*, **619**, A148
 Paxton, B., Bildsten, L., Dotter, A., et al. 2011, *ApJS*, **192**, 3
 Paxton, B., Cantiello, M., Arras, P., et al. 2013, *ApJS*, **208**, 4
 Paxton, B., Marchant, P., Schwab, J., et al. 2015, *ApJS*, **220**, 15
 Paxton, B., Schwab, J., Bauer, E. B., et al. 2018, *ApJS*, **234**, 34
 Peter, D., Feldt, M., Henning, T., & Hormuth, F. 2012, *A&A*, **538**, A74
 Raguzova, N. V., & Popov, S. B. 2005, *A&AT*, **24**, 151
 Rameau, J., Chauvin, G., Lagrange, A. M., et al. 2013, *ApJL*, **772**, L15
 Salaris, M., & Bedin, L. R. 2018, *MNRAS*, **480**, 3170
 Schlafly, E. F., & Finkbeiner, D. P. 2011, *ApJ*, **737**, 103
 Seager, S., & Sasselov, D. D. 1998, *ApJL*, **502**, L157
 Serabyn, E., Liewer, K., & Mawet, D. 2016, *OptCo*, **379**, 64
 Service, M., Lu, J. R., Campbell, R., et al. 2016, *PASP*, **128**, 095004
 Servillat, M., Tang, S., Grindlay, J. E., & Los, E. 2012, in Proceedings of “An INTEGRAL view of the high-energy sky (the first 10 years)” - 9th INTEGRAL Workshop and celebration of the 10th anniversary of the launch (INTEGRAL 2012) (Trieste: SISSA)
 Shrader, C. R., Hamaguchi, K., Sturmer, S. J., et al. 2015, *ApJ*, **799**, 84
 Sigurdsson, S., Richer, H. B., Hansen, B. M., Stairs, I. H., & Thorsett, S. E. 2003, *Sci*, **301**, 193
 Starovoit, E. D., & Rodin, A. E. 2017, *ARep*, **61**, 948
 Tauris, T. M., & van den Heuvel, E. P. J. 2006, in Compact Stellar X-ray Sources, ed. W. Lewin & M. van der Klis, Vol. 39 (Cambridge: Cambridge Univ. Press), 623
 Uyama, T., Ren, B., Mawet, D., et al. 2020, *AJ*, **160**, 283
 Viehmann, T., Eckart, A., Schödel, R., et al. 2005, *A&A*, **433**, 117
 Welsh, W. F. 2013, *Natur*, **499**, 33
 Williams, B. F., Durbin, M. J., Dalcanton, J. J., et al. 2021, *ApJS*, **253**, 53
 Wizinowich, P., Acton, D. S., Shelton, C., et al. 2000, *PASP*, **112**, 315
 Wolszczan, A., & Frail, D. A. 1992, *Natur*, **355**, 145
 Yan, Z., Shen, Z.-Q., Yuan, J.-P., et al. 2013, *MNRAS*, **433**, 162
 Zacharias, N., Finch, C. T., Girard, T. M., et al. 2012, *yCat*, **I/322A**